

A Numerical Study of Near Inertial Motions in Mid-Atlantic Bight Area Induced by Hurricane Irene (2011)

Peida Han¹ and Xiping Yu²

Abstract

Hurricane Irene generated strong near inertial currents (NICs) in the ocean waters when passing over the Mid-Atlantic Bight (MAB) of the U. S. East Coast in late August 2011. It is demonstrated that a combination of the valuable field data with detailed model results can be exploited to study the development and decay mechanism of this event. Numerical results obtained with regional oceanic modeling system (ROMS) are shown to agree well with the field data. Both computed and observed results show that the NICs were significant in most areas of the MAB region except in the nearshore area where the stratification was totally destroyed by the hurricane-induced strong mixing. Based on the energy budget, it is clarified that the near inertial kinetic energy (NIKE) was mainly gained from the wind power during the hurricane event. In the deep water region, NIKE was basically balanced by the vertical turbulence diffusion (40%) and downward divergence (33%). While in the continental shelf region, NIKE was mainly dissipated by the vertical turbulence diffusion (67%) and partially by the bottom friction (24%). Local dissipation of NIKE due to turbulence diffusion is much more closely related to the rate of the vertical shear rather than the intensity of turbulence. The strong vertical shear at the offshore side of the continental shelf led to a rapid dissipation of NIKE in this region.

Keywords: Hurricane Irene (2011); Mid-Atlantic Bight; Near inertial current; Energy budget; Timescale of near inertial energy decay

¹ PhD Candidate. Department of Hydraulic Engineering, Tsinghua University, Beijing, China.

² Corresponding Author. Professor. Department of Ocean Science and Engineering, Southern University of Science and Technology, Shenzhen, China. Email: yuxp@sustech.edu.cn

23 1. Introduction

24 Near inertial currents (NICs), observed widely in ocean basins around the world, are
25 characterized by the important role of Coriolis effect and by the periodic motion with the
26 frequency of an inertial mode (Garrett, 2001). The basic energy source of these freely
27 flowing currents is the wind power (Pollard, 1980; D'Asaro et al., 1985). Globally, the
28 annually averaged wind power supply to NICs was estimated ranging from 0.3 TW to more
29 than 1 TW by previous investigators (Alford, 2003a; Furuichi et al., 2008; Rimac et al.,
30 2013). As a comparison, the total power required to maintain the abyssal stratification and
31 the thermohaline circulation is about 2 TW (Munk and Wunsch, 1998). This implies that
32 NIC is a very important phenomenon in physical oceanography (Gregg, 1987; Alford, 2003b;
33 ~~Jochum et al., 2013). In fact, NICs are believed to have a significant role in upper-ocean~~
34 ~~mixing, which may substantially affect the thermohaline circulation and even modulate the~~
35 ~~climate (Gregg, 1987; Alford, 2003b; Jochum et al., 2013).~~

36 A tropical or an extratropical cyclone (hereinafter collectively referred as TC) is a
37 rotating low-pressure and strong-wind mesoscale weather system, which generates NICs
38 more powerfully than other types of atmospheric processes in nature (Alford et al., 2016;
39 Steiner et al., 2017). When a TC passes over a deep ocean, enormous energy is directly
40 transferred into the ocean waters, which rapidly generates strong NICs with a velocity up to
41 1 m/s in the horizontal direction of the mixed layer (Price, 1983; Sanford et al., 2011). Right-
42 bias effect is often shown in the NIC pattern, i.e., NICs are more intense on the right side of
43 the hurricane track, due to the resonance between the surface flow driven by NICs and
44 clockwise rotating wind stress on the right side (Chang and Anthes, 1978; Price, 1994).
45 After the passage of a TC, the surface near inertial energy usually persists for several inertial
46 cycles, and then gradually decays (Price, 1983; Sanford et al., 2011; Hormann et al., 2014;
47 Zhang et al., 2016; Wu et al., 2020).

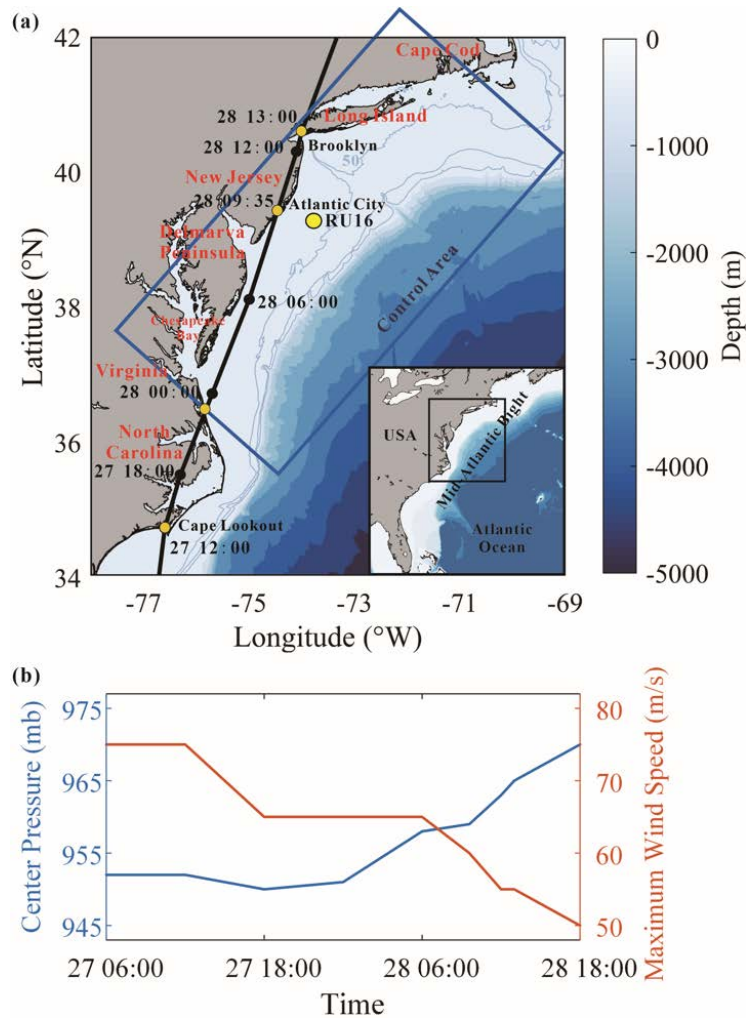
48 It is known that NICs in shallow waters show some significant differences with those
49 in deep waters and the velocity of NICs in shallow waters is usually of a smaller magnitude
50 of 0.1-0.5 m/s (Chen and Xie, 1997; Rayson et al., 2015; Yang et al., 2015; Chen et al., 2017;

51 Zhang et al., 2018). The decrease of current velocity in shallow waters may be an effect of
52 the sea-bottom friction as Rayson et al. (2015) pointed out. Chen and Xie (1997), however,
53 found that it was because a significant part of the wind input, which may otherwise be an
54 energy source of the NICs, was exhausted to generate a wave-induced nearshore current
55 system. Chen et al. (2017) considered that barotropic waves in the shallow waters, such as
56 seiches, may trap some wind energy. In addition to the difference in magnitude, the modes
57 of the NICs in shallow and deep waters are also different. More specifically, a two-layer
58 structure was observed in shallow waters in several studies, i.e., NICs were in opposite
59 phases in surface and bottom layers, which differed from the conventional multi-layer mode
60 in deep waters (Chen et al., 1996; Shearman, 2005; Yang et al., 2015), though a multi-layer
61 mode may also be observed sometimes in nearshore waters due to combined effect of
62 changing wind stress, variable stratification and nonlinear bottom friction (Mackinnon and
63 Gregg, 2005).

64 There have been a considerable number of studies on the decay of specific TC
65 generated NICs in coastal regions. Rayson et al. (2015) paid attention to four intense TCs
66 on the Australian North-West Shelf and related the rapid decay of NICs in shallow waters
67 to the bottom friction. Yang et al. (2015) examined coastal ocean responses to Typhoon
68 Washi and found that the negative background vorticity could trap near inertial energy and
69 result in a slow decay. Shen et al. (2017) investigated five TCs over the Taiwan Strait and
70 identified a rapid decaying rate due to nonlinear interaction between NICs and tides. Zhang
71 et al. (2018) studied Hurricane Arthur in Mid-Atlantic Bight and showed that excessive wind
72 input does not necessarily lead to amplification of NICs because intensive wind input is
73 usually accompanied by an even higher rate of energy dissipation.

74 Though a significant number of investigations have been conducted, some basic
75 features of a TC induced NIC in the coastal ocean are still not clarified. For instance, the
76 energy budget in the NIC generated by a TC has not yet been thoroughly discussed in either
77 deep or shallow waters; and the relative importance of different physical processes including
78 advection, conversion, turbulence diffusion, bottom friction, energy divergence, etc., in the

79 energy budget has not yet been fully understood. In addition, it is still not concluded on
 80 which processes dominate the decay of near inertial energy or on how each physical process
 81 affects the decay rate of the near inertial energy in deep and shallow waters, respectively.
 82 Our limited understanding to the basic features of a TC induced NIC is largely due to the
 83 difficulties in ocean observations under extreme weather.
 84



85
 86 Figure 1. (a) Map of the MAB region. Best track of Hurricane Irene (2011) reported by Avila
 87 and Cangialosi (2011) is shown by a black line. Reanalysis data provided by H*WIND
 88 shows a similar track with Avila and Cangialosi (2011) and is thus omitted. The mean
 89 position of Glider RU16 is marked by a yellow circle. The control domain defined in Section
 90 4 is marked by a blue box. (b) Time series of center pressure and 10-m maximum wind
 91 speed of Hurricane Irene reported by Avila and Cangialosi (2011).
 92

93 In this study, we pay a close attention to the NIC induced by Hurricane Irene (2011).
 94 Hurricane Irene (2011) crossed over the Mid-Atlantic Bight (MAB), a coastal region of the
 95 North Atlantic, extending from Cape Cod, Massachusetts to Cape Lookout, **North Carolina**,
 96 USA, as shown in Figure 1a. Before the hurricane event, seawater stratification in MAB
 97 was quite strong due to the Cold Pool effect (Lentz, 2017) and the temperature difference
 98 between the surface and the bottom exceeded 10 °C. **The vertical gradient of the temperature**
 99 **should also be very large because previous studies showed that the thermocline in shelf**
 100 **region was rather thin; for instance, the thermocline was less than 5 m in the place where**
 101 **water depth was around 40 m (Glenn et al., 2016; Seroka et al., 2017).** During the passage
 102 of Hurricane Irene (2011), a network of High-frequency (HF) radars measured the surface
 103 currents in MAB (Roarty et al., 2010). Meanwhile, a Slocum glider launched near New
 104 Jersey measured the vertical profiles of the temperature and the salinity (Schofield et al.,
 105 2010). Combination of the valuable field data with effective numerical techniques then
 106 provided an opportunity to achieve a comprehensive study of the NICs generated by this
 107 hurricane event.

108 **2. Numerical Model**

109 **2.1 Basic Equations**

110 In this study, the ocean responses to Hurricane Irene (2011) are studied using the
 111 regional oceanic modeling system (ROMS) (Shchepetkin and McWilliams, 2005;
 112 Haidvogel et al., 2008). ROMS deals with the Reynolds-averaged N-S equations in the σ
 113 coordinate system (Freeman et al., 1972). Specifically, the Cartesian coordinate z is
 114 replaced by σ based on a general relation $\chi(\sigma) = (z - \eta) / D$, where η is the vertical
 115 displacement of the free surface and D is the instantaneous water depth, while $\chi(\sigma)$ is
 116 a stretching function introduced for grid refinement. In the σ -coordinate system the
 117 Reynolds-averaged N-S equations may finally be expressed as

$$118 \quad \frac{\partial \xi}{\partial t} + \frac{\partial(\xi u)}{\partial x} + \frac{\partial(\xi v)}{\partial y} + \frac{\partial(\xi \omega)}{\partial \sigma} = 0 \quad (1)$$

$$\begin{aligned}
119 \quad & \frac{\partial(\xi u)}{\partial t} + \frac{\partial(\xi uu)}{\partial x} + \frac{\partial(\xi uv)}{\partial y} + \frac{\partial(\xi u\omega)}{\partial \sigma} - f\xi v + \frac{\xi}{\rho} \frac{\partial p}{\partial x} \\
& = -g\xi \left(\chi \frac{\partial D}{\partial x} + \frac{\partial \eta}{\partial x} \right) + \frac{\partial}{\partial \sigma} \left(\frac{\nu}{\xi} \frac{\partial u}{\partial \sigma} \right) + \frac{\partial}{\partial x} \left(\xi \nu' \frac{\partial u}{\partial x} \right) + \frac{\partial}{\partial y} \left(\xi \nu' \frac{\partial u}{\partial y} \right)
\end{aligned} \tag{2}$$

$$\begin{aligned}
120 \quad & \frac{\partial(\xi v)}{\partial t} + \frac{\partial(\xi uv)}{\partial x} + \frac{\partial(\xi vv)}{\partial y} + \frac{\partial(\xi v\omega)}{\partial \sigma} + f\xi u + \frac{\xi}{\rho} \frac{\partial p}{\partial y} \\
& = -g\xi \left(\chi \frac{\partial D}{\partial y} + \frac{\partial \eta}{\partial y} \right) + \frac{\partial}{\partial \sigma} \left(\frac{\nu}{\xi} \frac{\partial v}{\partial \sigma} \right) + \frac{\partial}{\partial x} \left(\xi \nu' \frac{\partial v}{\partial x} \right) + \frac{\partial}{\partial y} \left(\xi \nu' \frac{\partial v}{\partial y} \right)
\end{aligned} \tag{3}$$

$$121 \quad 0 = -\frac{1}{\rho} \frac{\partial p}{\partial \sigma} - g\xi \tag{4}$$

$$\begin{aligned}
122 \quad & \frac{\partial(\xi C)}{\partial t} + \frac{\partial(\xi uC)}{\partial x} + \frac{\partial(\xi vC)}{\partial y} + \frac{\partial(\xi \omega C)}{\partial \sigma} \\
& = \frac{\partial}{\partial \sigma} \left(\frac{\kappa}{\xi} \frac{\partial C}{\partial \sigma} \right) + \frac{\partial}{\partial x} \left(\xi \kappa' \frac{\partial C}{\partial x} \right) + \frac{\partial}{\partial y} \left(\xi \kappa' \frac{\partial C}{\partial y} \right)
\end{aligned} \tag{5}$$

123 where, $\xi = \partial z / \partial \sigma = D(\partial \chi / \partial \sigma)$; u , v , ω are the velocity components in x , y , σ
124 directions, respectively; C stands for the potential temperature T or salinity S ; p is
125 the seawater pressure; ρ is the density of the seawater; $f = 2\Omega \sin \phi$ is the Coriolis
126 parameter with $2\Omega = 1.458 \times 10^{-4} \text{ s}^{-1}$ and ϕ being the latitude; ν and κ are the
127 diffusion coefficients for momentum and potential temperature or salinity, respectively, in
128 the vertical direction; ν' and κ' are those in the horizontal directions; Note that Eq. (1)
129 is the continuity equation; Eqs. (2) and (3) are equations of motion in two horizontal
130 directions; Eq. (4) is the hydrostatic assumption; Eq. (5) is the advection-diffusion equation
131 of the potential temperature or the salinity. The density of the seawater ρ is determined
132 following the equation of state proposed by Jackett and McDougall (1995):

$$133 \quad \rho(S, T, p) = \frac{\rho_0}{1 - p/K(S, T, p)} \tag{6}$$

134 where $\rho_0 = \rho(S, T, 0)$ is the seawater density at the standard atmospheric pressure and
135 $K(S, T, p)$ is the bulk modulus, both are given by Jackett and McDougall (1995).

136 The vertical mixing is known to play an important role in determining the structure of
137 a NIC, so it must be properly evaluated. In this study, we consider $\nu = \nu_0 + \nu_e$ and

138 $\kappa = \kappa_0 + \kappa_e$, in which ν_0 and κ_0 are the molecular viscosity and diffusivity of the
139 seawater, set to $\nu_0 = 10^{-5} \text{ m}^2/\text{s}$ and $\kappa_0 = 10^{-6} \text{ m}^2/\text{s}$ following previous suggestions (Xu
140 et al., 2002; Li and Zhong, 2007; Lentz, 2017), while ν_e and κ_e are the eddy viscosity
141 and diffusivity, determined by the conventional k- ϵ turbulence model (see Rodi (1987) and
142 Umlauf and Burchard (2003) for detailed description), a widely employed model that
143 demonstrated good performance in simulating various oceanographic processes
144 (Olabarrieta et al., 2011; Toffoli et al., 2012; Zhang et al., 2018).

145 Horizontal mixing is included in Eqs. (2), (3) and (5), though it has been pointed out
146 to play a relatively insignificant role in simulating response of the stratified ocean to a
147 hurricane, as compared to vertical mixing (Li and Zhong, 2007; Zhai et al., 2009; Dorostkar
148 et al., 2010). In the ocean basin of the present interest, the horizontal diffusion coefficient
149 was estimated to be an order of $10 \text{ m}^2/\text{s}$ under extreme conditions, e.g., TC condition
150 (Allahdadi, 2014; Mulligan and Hanson, 2016). Thus, we take $\nu' = \kappa' = 10 \text{ m}^2/\text{s}$ in the
151 present study for simplicity to simulate the ocean response to Hurricane Irene.

152 2.2 Computational Conditions

153 In order to fully capture the NIC induced by Hurricane Irene (2011), our computational
154 domain covers the entire MAB regions of the U. S. East Coast extending from Cape Cod,
155 Massachusetts, to Cape Lookout, North Caroline. The computational domain is discretized
156 into 35 layers with refinement near the surface and covered with a $5 \text{ km} \times 5 \text{ km}$ grid in the
157 horizontal plane. The 1 arc-min bathymetry data is obtained from ETOPO1 Global Relief
158 Model (Amante and Eakins, 2009) and resampled to a resolution of 5 km. The simulation
159 starts from 20 August, one week before the hurricane event and lasted for a period of 16
160 days. The time step is set to 1 min.

161 The initial and open boundary conditions of the seawater temperature and salinity, the
162 ocean flow velocities and the sea surface elevation are all from the Hybrid Coordinate Ocean
163 Model (HYCOM, <https://www.hycom.org/>) with a resolution of $1/12^\circ$ in space and 3 hr in
164 time (Cummings, 2005; Chassignet et al., 2007). The initial stratification in the HYCOM is
165 examined through a comparison with the 4D data provided by Experimental System for

166 Predicting Shelf and Slope Optics (ESPreSSO, <http://www.myroms.org/espresso/>). Seven
 167 tidal constituents (M2, S2, N2, K2, O1, K1, Q1) included in the simulation are derived from
 168 the ADvanced CIRCulation model (ADCIRC, <https://adcirc.org/>). Daily inflows from the
 169 eleven largest rivers, containing Susquehanna River, Delaware River, Hudson River,
 170 Potomac River, etc., are obtained from the United States Geological Survey (USGS,
 171 <https://waterdata.usgs.gov/>). The so-called radiation-nudging condition is adopted at the
 172 open boundaries (Marchesiello et al., 2001). Wet-and-dry option is activated at coastal
 173 boundaries (Warner et al., 2013). The seabed boundary condition is required to satisfy:

$$174 \quad \nu \frac{\partial \mathbf{u}}{\partial z} = \boldsymbol{\tau}_b = \rho \left[\frac{\lambda}{\ln(\Delta z / z_0)} \right]^2 |\mathbf{u}_b| \mathbf{u}_b \quad (7)$$

175 where, $\boldsymbol{\tau}_b$ is the bottom friction; λ is the von Karman constant; \mathbf{u}_b is the fluid velocity
 176 at the center of the bottom layer; Δz is the distance between the center of the bottom layer
 177 and the seabed; z_0 is the bottom roughness, which is set to 0.02 m in MAB following
 178 Churchill et al. (1994).

179 The hurricane wind forcing required in this study can be obtained from two sources,
 180 i.e., the H*WIND data, with a spatial resolution of 6 km and a temporal resolution of 6 hr,
 181 published by Atlantic Oceanographic and Meteorological Laboratory, National Oceanic and
 182 Atmospheric Administration (AOML/NOAA) ([https://www.aoml.noaa.gov/hrd/data_sub/](https://www.aoml.noaa.gov/hrd/data_sub/wind.html)
 183 [wind.html](https://www.aoml.noaa.gov/hrd/data_sub/wind.html)) (Powell et al., 1998) and the North American Mesoscale (NAM) data, with a
 184 spatial resolution of 12 km and a temporal resolution of 3 hr, provided by National Centers
 185 for Environmental Prediction (NCEP) ([https://www.ncdc.noaa.gov/data-access/model-](https://www.ncdc.noaa.gov/data-access/model-data/model-datasets/north-american-mesoscale-forecast-system-nam)
 186 [data/model-datasets/north-american-mesoscale-forecast-system-nam](https://www.ncdc.noaa.gov/data-access/model-data/model-datasets/north-american-mesoscale-forecast-system-nam)) (Janjic et al., 2004).
 187 In our computation, the former is used between 26 and 31 August (during the hurricane
 188 event) because it has a better accuracy in capturing the maximum wind speed, while the
 189 latter is used during other periods of the simulation. Reanalysis data for other atmospheric
 190 forcing, such as the surface air temperature, air pressure, relative humidity, radiation and
 191 precipitation are also available from NAM for determining the surface buoyancy fluxes. In
 192 particular, the wind drag τ_s , which is measure of the momentum flux can be estimated

193 through (Fairall et al., 1996):

$$194 \quad \tau_s = \rho_a C_d u_{10}^2 \quad (8)$$

195 where, ρ_a is the density of the air; C_d is the drag coefficient; u_{10} is the horizontal wind
 196 speed at the 10-m level; Several studies have confirmed that C_d does not increase but level
 197 off or even decrease at high wind speeds (Emanuel, 1995; Powell et al., 2003; Donelan et
 198 al., 2004). Besides, C_d could be altered due to wave deformation in response to
 199 bathymetry change, especially in coastal regions (Chen et al., 2018; Xu and Yu, 2021). **In
 200 order to correctly represent the effect of the air-sea interactions under extreme wind
 201 conditions, we choose an empirical formula which fits the numerical results obtained with
 202 the improved wave boundary layer model developed by Chen and Yu (2016), Chen et al.
 203 (2018) and Xu and Yu (2021):**

$$204 \quad C_d = C_{dw} + \frac{C_{d0} - C_{dw}}{(W_0 - W)^2} (u_{10} - W)^2 \quad (9)$$

205 where C_{d0} is a threshold value set to 0.001 for the wind stress at $u_{10} \leq W_0 = 5$ m/s, C_{dw}
 206 is the saturated wind stress coefficient and W is the saturation wind speed. We have

$$207 \quad C_{dw} = \begin{cases} -1.86 \times 10^{-4} \ln \frac{gD}{W_D} + 0.0025 & \frac{gD}{W_D} \leq 3 \\ 0.00225 & \frac{gD}{W_D} > 3 \end{cases} \quad (10)$$

$$208 \quad W = \begin{cases} 4.64 \ln \left(\frac{gD}{W_D} \right) + 42.6 & \frac{gD}{W_D} \leq 0.6 \\ W_D & \frac{gD}{W_D} > 0.6 \end{cases} \quad (11)$$

209 where W_D set to 40 m/s is the saturation wind speed in deep water. Except for the
 210 momentum flux, other air-sea fluxes, e.g., the sensible heat flux and the latent heat flux, are
 211 determined based on the conventional bulk parameterization scheme (see Fairall et al. (1996)
 212 for detailed description). **The sea surface boundary condition is then required to satisfy:**

$$213 \quad \nu \frac{\partial \mathbf{u}}{\partial z} = \tau_s \quad (12)$$

214 2.3 Observational data

215 During the passage of Hurricane Irene (2011), a network of High-frequency (HF)
216 radars measured the surface currents and a Slocum glider launched near New Jersey
217 measured the vertical profiles of the temperature and the salinity (Roarty et al., 2010;
218 Schofield et al., 2010). The measured data are used to verify the computational results in
219 this study. In fact, they have been widely used in previous studies (Glenn et al., 2016; Seroka
220 et al., 2016; Seroka et al., 2017).

221 HF Radars in the Mid-Atlantic Regional Association's Coastal Ocean Observing
222 System (MARACOOS, <https://maracoos.org/>) are able to observe the surface currents. The
223 recorded data have a temporal resolution of 1 hr and a spatial resolution of 6 km, and are
224 assumed to be measured at an effective depth of around 2.7 m below the ocean surface based
225 on Roarty et al. (2020). The data cover the MAB area from the coast to the shelf break and
226 have a reasonably good accuracy. In fact, they show a RMS difference within 8 cm/s when
227 compared with data measured by ADCP (Roarty et al., 2010; Roarty et al., 2020).

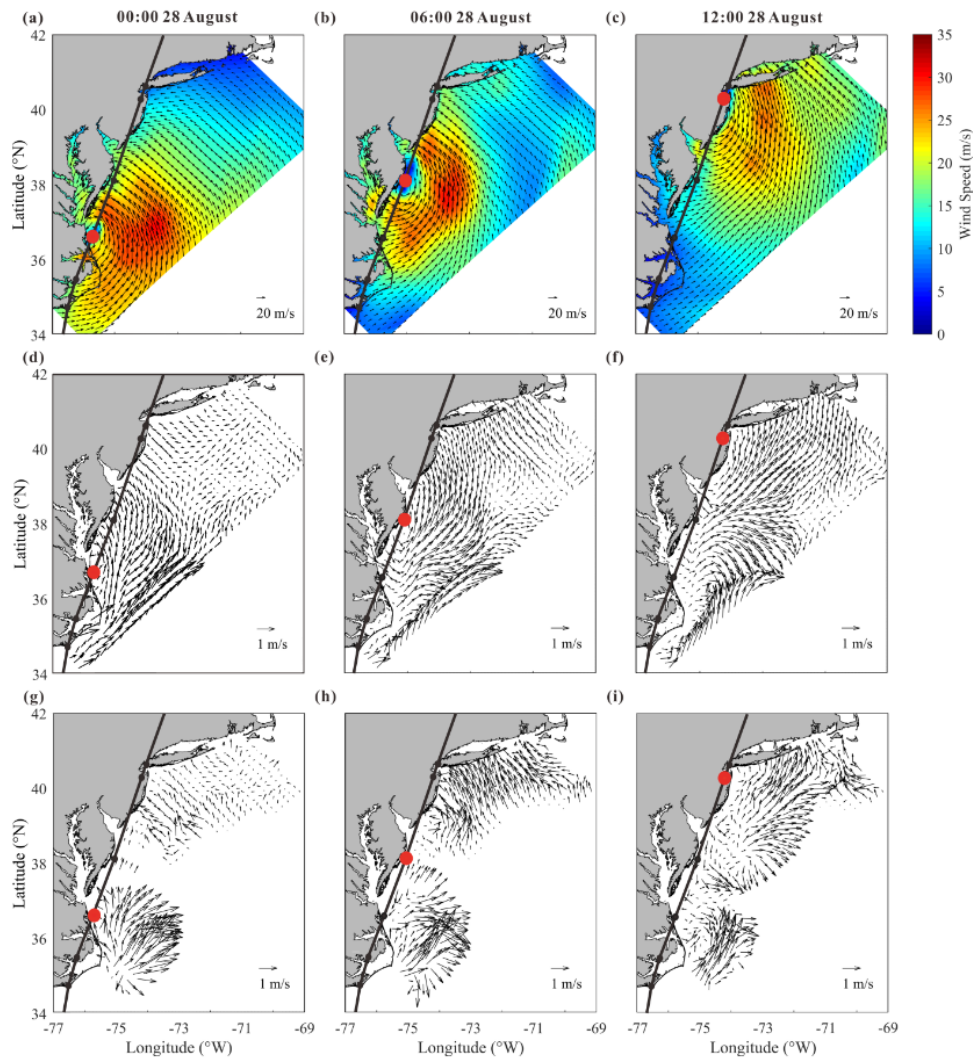
228 Glider RU16 was an autonomous underwater vehicle of the Rutgers Slocum glider
229 (Schofield et al., 2007, 2010) platform developed by Teledyne-Webb Research
230 (<https://rucool.marine.rutgers.edu/data/underwater-gliders>), and has demonstrated to be
231 advantageous in marine monitoring, particularly under extreme weather conditions (Glenn
232 et al., 2016; Miles et al., 2017; Seroka et al., 2016; Seroka et al., 2017; Zhang et al., 2018).
233 It was equipped with the Seabird un-pumped conductivity, temperature, and depth (CTD)
234 sensor, and could thus measure not only the vertical profiles of the seawater temperature
235 and the salinity but also the water depth. It was programmed to move vertically through the
236 water column, collect data every 2 s, and surface at a 3 h interval to provide high temporal
237 resolution data (Schofield et al., 2007; Glenn et al., 2016; Seroka et al., 2016).

238 3 Ocean Responses to Hurricane Irene

239 3.1 Effect of hurricane on ocean surface flow

240 As shown in Figure 1, Hurricane Irene (2011) entered the Mid-Atlantic Bight (MAB)

241 area of the present interest at Cape Lookout, North Carolina as a Category-1 event at 12:00,
 242 27 August, 2011 (UTC time, the same below) with a maximum sustained wind (MSW) of
 243 over 38 m/s. It continued to move northeastward and made a landfall at Atlantic City, New
 244 Jersey at 9:35, 28 August with a MSW of around 30 m/s. During its motion in the MAB area
 245 of our interest, the radius of the hurricane wind field (the area with wind speed ≥ 32.9 m/s)
 246 reached a large value of 140 km (Avila and Cangialosi, 2011).
 247



248
 249 Figure 2. Snapshots of (a-c) the 10-m wind provided by H*WIND, (d-f) computed current
 250 velocity of the surface layer and (g-i) observed current velocity of the surface layer, at (left
 251 column) 00:00, (middle column) 06:00 and (right column) 12:00, 28 August, during the
 252 passage of Hurricane Irene (2011). Note that best track of the hurricane reported by Avila
 253 and Cangialosi (2011) is shown by black lines while the hurricane center is shown by red
 254 circles.

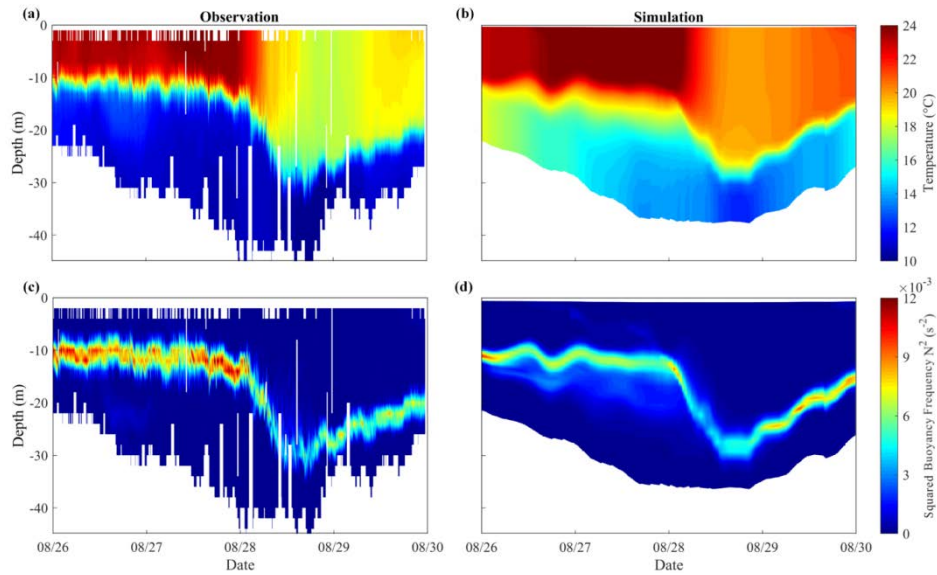
255 Figure 2 provides the snapshots of the wind, the computed and observed currents in
256 the MAB area at 00:00, 06:00 and 12:00, 28 August, 2011, respectively. Note that 00:00 and
257 12:00 correspond to the time when Hurricane Irene entered and left the area of our interest,
258 respectively. The wind field is plotted from the H*WIND data, while ~~the field currents are
259 obtained from the HF Radars and detided. by analyzing data from Field currents are obtained
260 by analyzing data from a network of High-Frequency Radar (HF Radar) stations (Roarty et
261 al., 2010) in the Mid-Atlantic Regional Association's Coastal Ocean Observing System. The
262 field data have a temporal resolution of 1 hr and a spatial resolution of 6 km, and are
263 assumed to be measured at an effective depth of 2.4 m below the ocean surface. The data
264 cover the MAB area from the coast to the shelf break and demonstrate a reasonably good
265 accuracy when compared to data obtained with ADCP (Acoustic Doppler Current Profiler),
266 which are usually considered to be reliable (Liu et al, 2014).~~

267 The computed current velocity of the surface layer, as shown in Figure 2d-f, is
268 compared with the observed one, as shown in Figure 2g-i, to verify the reliability of the
269 numerical model presented in this study. At 00:00, 28 August, it is numerically demonstrated
270 that currents rotating counterclockwise with a magnitude of over 1 m/s are rapidly generated
271 by the wind near the hurricane center (Figure 2d). In the observed results, though there are
272 significant data missing near the hurricane center, northeastward currents can still be
273 identified on the offshore waters along North Carolina coast (Figure 2g) and are in
274 reasonable agreement with the computed current field. Moreover, both computational and
275 observational results support a fact that the onshore wind (Figure 2a) on the front side of the
276 hurricane drives an onshore current with magnitude of 0.4 m/s along the northern MAB,
277 especially in the nearshore area of New Jersey (Figure 2d and 2g). At 06:00, Hurricane Irene
278 arrived at the offshore waters of Delmarva Peninsula. In spite of the field data missing, the
279 rotating currents induced by the hurricane wind can be clearly recognized in both computed
280 and observed results in the nearshore area of New Jersey (Figure 2e and 2h). In addition,
281 relatively strong onshore currents with magnitude of over 1 m/s are observed near Long
282 Island and are also well represented in the numerical results (Figure 2e). At 12:00, i.e., the

283 time when the hurricane left the area of our interest, the counterclockwise rotating currents
284 are still formed near the hurricane center as demonstrated by both computational and
285 observational results (Figure 2f and 2i). At the same time, clockwise rotating currents are
286 shown to be generated near Delmarva Peninsula in southern MAB after the hurricane passed
287 over. This fact is certainly confirmed by both computed and observed results, indicating
288 near inertial currents are activated after the hurricane event. Therefore, it becomes evident
289 that the rotating wind of the hurricane immediately forces a rotating current in the surface
290 layer of the ocean and induces an inertial current rotating in the opposite direction shortly
291 after the hurricane passed over. It is also worthwhile to emphasize that, in general, the
292 numerical results obtained with the present model agree fairly well with observed data.

293 3.2 Effect of hurricane on vertical stratification and sea surface cooling

294 Shown in Figure 3a is the vertical profile of the seawater temperature measured by
295 Glider RU16 launched off the New Jersey Coast. ~~Glider RU16 was an autonomous~~
296 ~~underwater vehicle of the Slocum glider platform developed by Teledyne Webb Research~~
297 ~~(Schofield et al., 2007, 2010), which has demonstrated to be advantageous in marine~~
298 ~~monitoring, particularly under extreme weather conditions (Glenn et al., 2016; Miles et al.,~~
299 ~~2017; Seroka et al., 2016; Zhang et al., 2018). Glider RU16 can measure not only the vertical~~
300 ~~profiles of seawater temperature and salinity but also the water depth. During the hurricane~~
301 ~~event, its position may include a certain amount of drift in the horizontal directions due to~~
302 ~~the ambient flow.~~ In Figure 3a, it is seen that the mixed layer off New Jersey coast was quite
303 thin, with a thickness of less than 10 m, before the hurricane event. A strong stratification
304 was clearly formed over a water depth of 40 m, with a surface temperature of 24 °C and a
305 bottom temperature of 10 °C. When the hurricane center passed over the position of Glider
306 RU16 at around 09:30, 28 August, the thickness of the mixed layer rapidly increased to
307 nearly 30 m while the surface temperature was decreased by more than 5 °C, indicating a
308 strong mixing process has occurred. By plotting the time series of the squared buoyancy
309 frequency N based on the measured data, expansion of the mixed layer due to the
310 hurricane event may be more vividly demonstrated (Figure 3c).



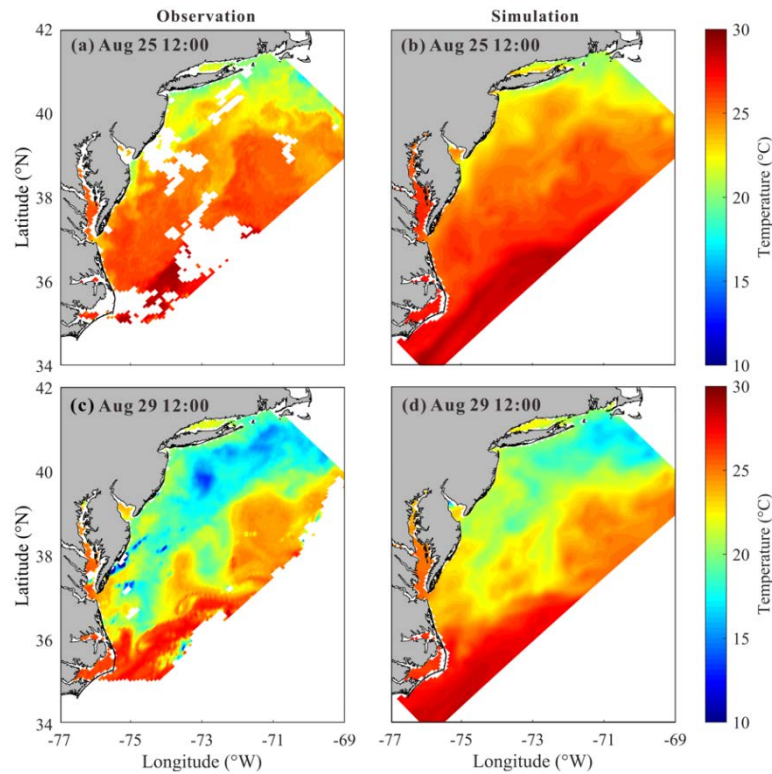
311

312 Figure 3. Time series of the vertical profiles of (top row) the temperature and (bottom row)
 313 the squared buoyancy frequency, obtained from (a, c) Glider RU16 and (b, d) numerical
 314 model.

315

316 Figure 3b and 3d present the computed results for the vertical distribution of seawater
 317 temperature obtained by virtually setting a measuring point moving with the glider in the
 318 real situation. The numerical results show a similar variation of the stratification pattern
 319 before and during the hurricane event, indicating that the numerical model is capable of
 320 describing the development and destruction of ocean stratification. However, a sea surface
 321 cooling of about 4 °C obtained by the numerical model is a little smaller than 6-7 °C
 322 observed by the glider in the field, probably due to the inaccurate setting of the initial bottom
 323 temperature in the computation. **Discrepancies of the squared buoyancy frequency N was**
 324 **also found in the thermocline (Figure 3c), where the temperature varied most dramatically.**
 325 **They are probably caused by the inaccurate setting of the initial temperature profile.** In fact,
 326 the initial condition for the bottom temperature in HYCOM is somehow higher (about 4°C)
 327 than the observed value in the field if Figures 3a and 3b are compared. To correct this system
 328 error, the real-time profile obtained from RU16 is used for a nudging process in computation,
 329 i.e., the model temperature and salinity fields are forced to nudge toward observed data (see
 330 Thyng et al. (2021) for detailed description).

331



332

333 Figure 4. Sea surface temperature at Aug 25 12:00, before the hurricane event (top row) and
 334 at Aug 29 12:00, after the hurricane event (bottom row) from (a, c) observed data and (b, d)
 335 numerical model.

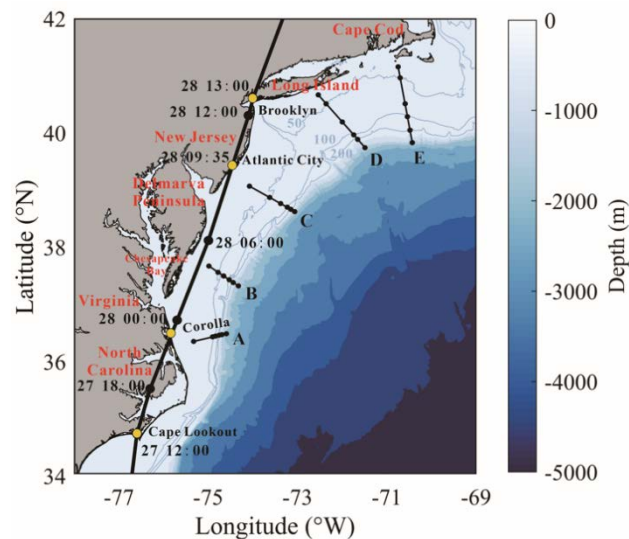
336

337 The sea surface temperatures (SST) before and after the hurricane event are further
 338 compared in Figure 4 (obtained from The Advanced Very High Resolution
 339 Radiometer (AVHRR), <https://earth.esa.int/eogateway/catalog/avhrr-level-1b-local-area-coverage-imagery>). Before the hurricane event, both observed and computed SST show
 340 similar patterns, i.e., the SST decreases with the increasing latitude. **After the hurricane**
 341 **passage, the strong mixing and cooling mainly take place in shallow waters, where the initial**
 342 **stratification is strong (Zhang et al., 2016), especially near New Jersey and Long Island.**
 343 **However, the cooling is not prominent in shallow waters near North Carolina. In fact, it has**
 344 **been reported that the SST in this region had decreased and then recovered to its pre-**
 345 **hurricane level within only 1 day (Seroka et al., 2016). The HYCOM data showed that the**
 346 **initial bottom temperature near North Carolina was as high as 18 °C. Therefore, little Cold**
 347 **Pool water in this region may have caused insignificant cooling and fast recovering.**
 348

349 It should be pointed out that the computed SST cooling is 3-4 °C smaller than the
 350 observed one, which could also be explained by the inaccurate initial condition obtained
 351 from HYCOM. The HYCOM bottom temperature is somehow higher than actual, which
 352 could lead to the underestimation of the SST cooling. Therefore, we use the real-time SST
 353 data obtained from AVHRR for nudging process in computation to correct this system error
 354 (Thyng et al., 2021), **considering that the accuracy of the initial stratification could**
 355 **obviously affect the modeling of mixing process.** Note that the error is mainly caused by the
 356 discrepancy in initial settings but not the defects in numerical method. Thus this error could
 357 be calibrated in certain extent and thus would not affect the reliability of subsequent analysis,
 358 e.g. energy budget analysis.

359 3.3 Characteristics of NIC

360 To have a general understanding of the NICs in the MAB area induced by Hurricane
 361 Irene (2011), a network of 30 stations aligned on 5 cross-shore sections from south to north
 362 is introduced in this study to cover the area of our interest as shown in Figure 5, similar to
 363 Zhang et al (2018). In each section, 6 stations are placed in the cross-shore direction from
 364 the shore side to the deep ocean, where water depths are around 30 m, 50 m, 75 m, 120 m,
 365 and 220 m and 1000 m, respectively. Note that the most offshore stations are located outside
 366 the shelf break.



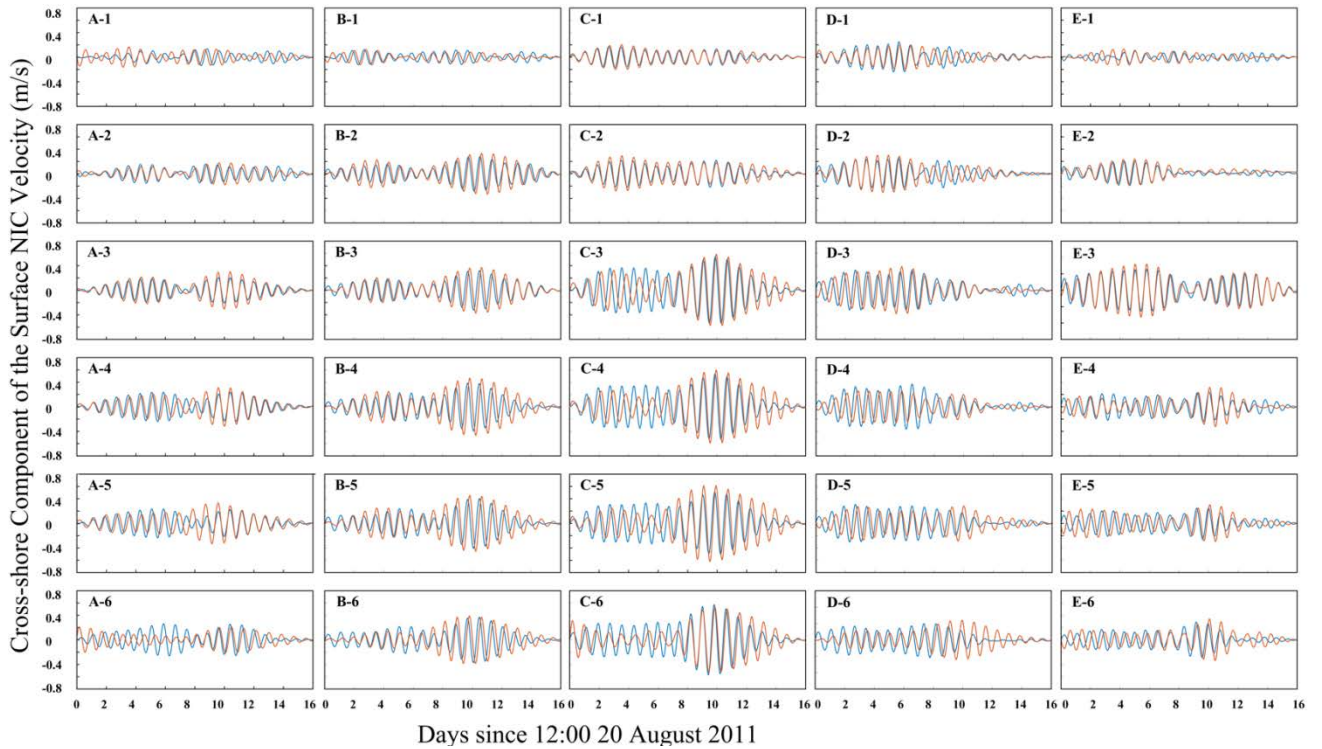
367
 368 **Figure 5. Five virtual sections marked by short black lines.**

369 The velocity of NIC is obtained from the total current velocity by first excluding the
370 tidal components and then passing it through a Butterworth filter with the frequency band
371 of $0.8-1.2 f_0$, an effective approach proposed by Hormann et al. (2014), Zhang et al. (2018)
372 and Kawaguchi et al. (2020). Shown in Figure 6 are the time series of surface velocity of
373 the NIC component in the cross-shore direction at all stations during the time period of our
374 study (16 days from 20 August to 5 September). The alongshore component was similar to
375 cross-shore component and thus omitted here. **It is demonstrated that the numerical results
376 are in reasonably good agreement with the HF Radar data and the Pearson product-moment
377 correlation coefficient reaches 0.7 (Derrick et al., 1994).** The major sources of error in the
378 measured data are found at the most offshore stations, such as A6 and D6, **where the
379 coverage of HF Radar is limited, i.e., at around 50 % (Roarty et al., 2010; Kohut et al. 2012).**
380 **Previous studies indicated that the observed data outside the shelf break with such a low
381 coverage should be used with caution (Roarty et al., 2010; Kohut et al. 2012; Roarty et al.
382 2020).** Error in the numerical results of the NICs may come from the minor errors in the
383 wind forcing data because they are very sensitively related, e.g., underestimation at C3-C6
384 before the hurricane event may come from the errors in low-resolution NAM data used in
385 pre-hurricane periods.

386 In Figure 6, it can be readily recognized that, in the cross-shore direction from shallow
387 to deep waters (i.e., Station No.1-No.5 in present study), the NIC velocity gradually
388 increases by a factor of at least three, e.g., from 0.15 m/s to 0.6 m/s in section C, which is
389 consistent with conclusions in previous studies (Kim and Kosro, 2013; Yang et al., 2015;
390 Rayson et al., 2015; Zhang et al., 2018). This is because that NIC velocity in the nearshore
391 region are restricted due to a combination of several reasons presented by Chen and Xie
392 (1997), Rayson et al. (2015) and Chen et al. (2017). Different from other studies, however,
393 the NIC velocity in the deep waters (i.e., Station No. 6 in the present study) is found to be
394 not larger or even smaller than that nearby the shelf break. This is probably due to that fact
395 that the track of Hurricane Irene (2011) was nearly attached to the shore during its motion
396 in the area of our interest and the wind stress over the deep ocean was relatively small. From

397 south to north, it is found that the NIC velocity in the middle regions, such as along section
 398 C, is larger than those in south and north. By checking the numerical results, it is found that
 399 the stratification was only slightly destroyed during the hurricane event near section C as
 400 compared to the adjacent sections, which thus provided a better environment for NIC
 401 generation (Yang et al., 2015; Shen et al., 2017).

402



403

404 Figure 6. Time series of the NIC velocity in the surface layer obtained (blue line) by the HF
 405 Radar and (orange line) with numerical model at 30 stations along sections A-E.

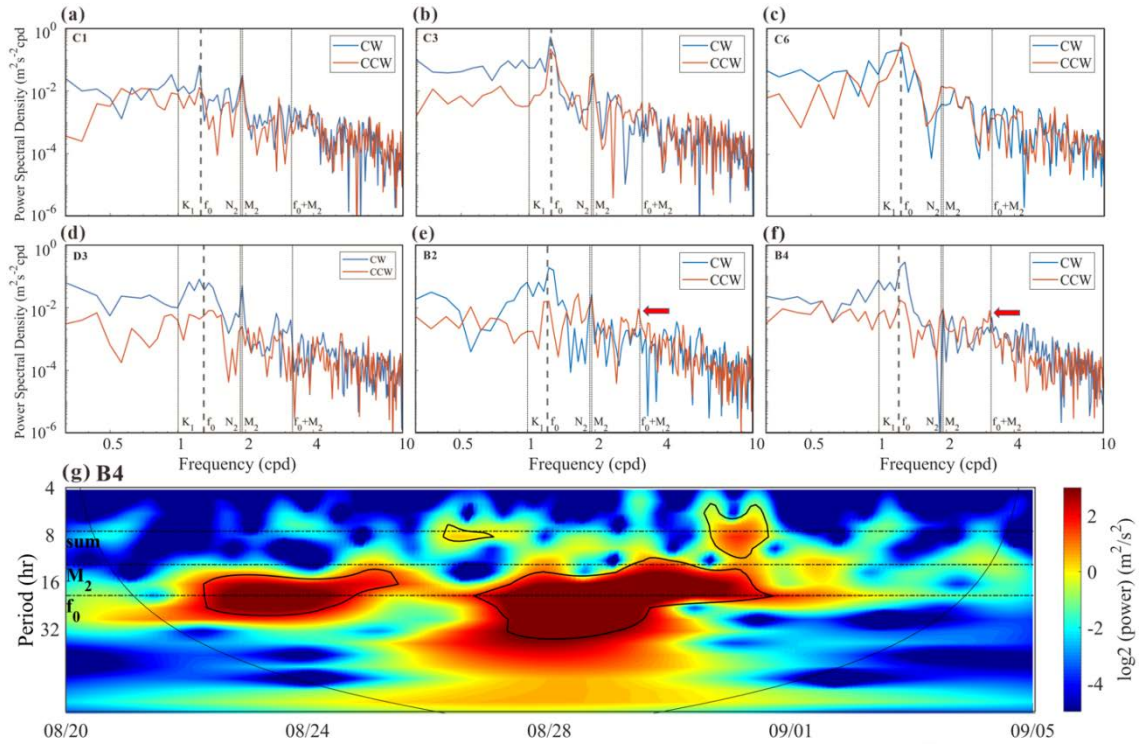
406

407 To evaluate the relative importance of the near inertial currents, the rotary spectra of
 408 the surface current velocity during the period of study (16 days) at different stations are
 409 shown in Figure 7. The tidal flows corresponding to the major constituents M2, N2 and K1,
 410 obtained with ADCIRC, are also plotted. It is seen that the velocity of the NICs is of an
 411 equivalent magnitude to that of the M2 tidal current at the shallow-water stations where the
 412 water depth is about 30 m (section C was taken for an example, Figure 7a). But, the velocity
 413 of the NICs is significantly larger than that of the tidal current in deeper regions (Figure 7b,
 414 c). It may be necessary to point out that weak NICs are not limited to the most nearshore

415 stations. In section D, for example, it is extended to a water depth of 75 m (Station D3,
416 Figure 7d). As discussed in the previous subsection, the weak NICs in the nearshore area
417 are closely related to the destruction of stratification by the strong mixing process associated
418 to the hurricane event (Yang et al., 2015; Shen et al., 2017). However, this effect does not
419 challenge the dominant role of NICs in deep waters.

420 Previous studies reported the nonlinear wave-wave interaction could transfer energy
421 from the M2 tide and NIC into a wave at the sum of their frequencies (f_{M2}). The key
422 mechanism is the coupling between the vertical shear in NIC and the vertical velocity due
423 to the internal tide (Davis and Xing, 2003; Hopkins et al., 2014; Shen et al., 2017; Wu et al.,
424 2020). Though the M2 tide is rather strong in shallow waters during the hurricane event
425 (Figure 7), nonlinear wave-wave interaction between the tidal current and the NIC could be
426 hardly identified in most part of MAB. Nevertheless, a peak of the energy spectrum seems
427 to appear at the sum-frequency f_{M2} for the surface velocity at Stations B1 to B4, near
428 Delmarva Peninsula (B2 and B4 were taken as examples in Figure 7e, f). The evolution of
429 energy power at different frequencies for the middle-layer averaged (i.e., 10-30 m) currents,
430 where the flow shear is concentrated, is further demonstrated based on wavelet analysis
431 (Station B4 was taken as an example in Figure 7g). A peak energy at the sum-frequency f_{M2}
432 is clearly identified after the hurricane passage. In fact, the subsequent Section 4.2 in this
433 paper will show that the strongest shear is found in offshore waters between Delmarva
434 Peninsula and New Jersey, i.e., near sections B and C (Figure 9a). Besides, Brunner and
435 Lwiza (2020) indicated that the most prominent M2 tide in southern MAB is located off
436 Delmarva Peninsula (near section B), according to a long-term observed data. Therefore,
437 the vertical shear in NIC and the vertical velocity due to the M2 tide is more likely to be
438 coupled in this region (i.e., near section B). However, this interaction only occurs in limited
439 regions and thus would not influence the NIC evolution in most part of MAB.

440



441

442 Figure 7. The rotary spectra of the current velocity in the surface layer during the simulation
 443 time (16 days) obtained by HF Radar at Stations (a) C1 (~30m), (b) C3 (~75m), (c) C6
 444 (~1000 m), (d) D3, (e) B2 and (f) B4. Clockwise and counter-clockwise components of the
 445 current are shown by blue and orange lines, respectively (NICs are considered to be
 446 dominated by the clockwise component). The frequencies of the major tidal constituents
 447 M2, N2 and K1, the inertial frequency f_0 , and the sum-frequency of M2 and f_0 are all marked
 448 by gray lines. (g) Wavelet power spectrum for 10-30 m depth-averaged alongshore current
 449 component at Station B4 (see Thiebaut and Vennell (2010) for detailed description). Black
 450 contours indicate the 5% significance level against red noise and the arc line indicate the
 451 cone of influence.

452 4 Near Inertial Kinetic Energy

453 4.1 Conservation of NIKE

454 For description of the intensity of a NIC, the near inertial kinetic energy (NIKE) may
 455 be defined in the following way:

456
$$E' = \frac{1}{2} \rho_0 |\mathbf{u}'|^2 \quad (13)$$

457 where, \mathbf{u}' is the velocity of the NIC; ρ_0 is the seawater density at the standard
 458 atmospheric pressure. Note that the NIKE is mainly gained from the wind power and
 459 dissipated due to a few mechanisms. Evolution of the vertically integrated NIKE within a
 460 water column from the sea bottom the ocean surface is thus governed by (Zhai et al., 2009)

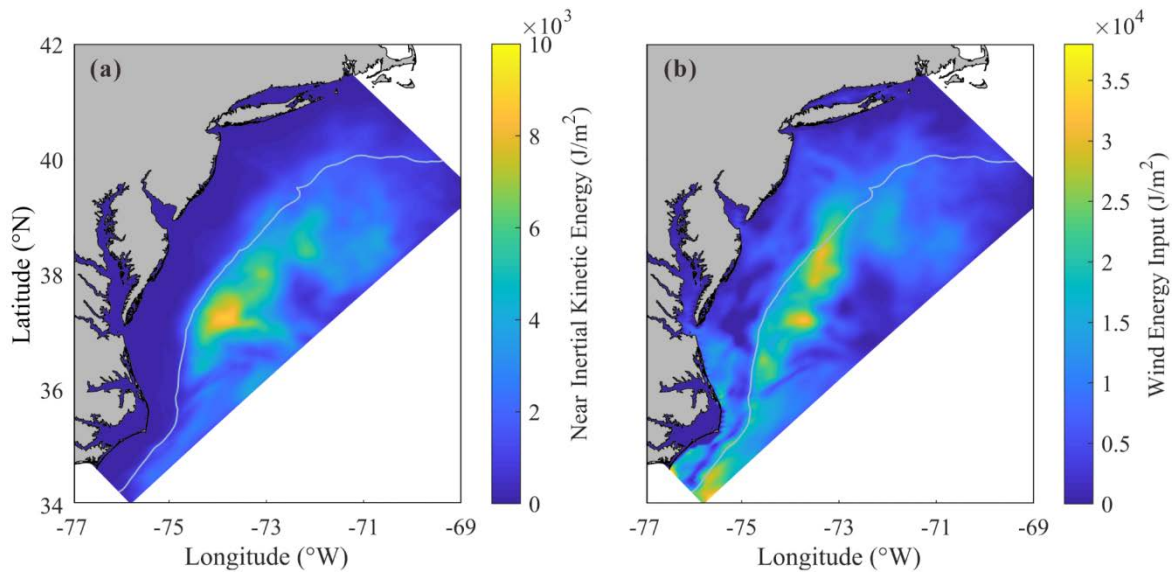
$$461 \quad \int_{-d}^{\eta} \frac{\partial E'}{\partial t} dz = \boldsymbol{\tau}_s \cdot \mathbf{u}'_s + \boldsymbol{\tau}_b \cdot \mathbf{u}'_b - \int_{-d}^{\eta} \rho_0 \nu_e \left| \frac{\partial \mathbf{u}'}{\partial z} \right|^2 dz - \quad (14)$$

$$\int_{-d}^{\eta} \nabla \cdot (\mathbf{u}' p') dz - \int_{-d}^{\eta} \rho' g w' dz - \int_{-d}^{\eta} \nabla \cdot (\mathbf{U} E') dz + \text{others}$$

462 where, \mathbf{u}'_s and \mathbf{u}'_b are near inertial velocities at sea surface and bottom, respectively; \mathbf{U}
 463 is the sub-inertial velocity; ρ' is the perturbation density, defined by $\rho' = \rho - \rho_*$; ρ_* is
 464 the reference density, i.e., the density corresponding to a flattened stratification where the
 465 fluid is redistributed adiabatically to a stable and vertically uniform state from the actual
 466 condition (Holliday and McIntyre, 1981; Kang and Fringer, 2010; MacCready and Giddings,
 467 2016); p' is the perturbation pressure, defined by $p' = g \int_z^{\eta} \rho' dz$. Terms on the right-hand
 468 side of Eq. (13) are the wind energy input, the dissipation due to bottom friction, the vertical
 469 diffusion due to turbulence, the horizontal divergence of near inertial energy flux, the
 470 conversion between kinetic and potential energy, and the advection of NIKE by the sub-
 471 inertial flow. The last term ‘others’ includes nonlinear transfer of energy between NICs and
 472 flows of other frequencies as well as the horizontal diffusion due to mixing. Note that the
 473 energy are integrated over the water column from $z = -d$ to free surface $z = \eta$. In
 474 shallow waters, d is the actual water depth, while in deep waters, d is truncated to 200
 475 m (i.e., the depth of the shelf break). When the bottom boundary is set at $z = -200$ m,
 476 the bottom friction vanishes in Eq. (13) but a term related to the downward energy flux, i.e.,
 477 $p' w' |_{z=-200m}$ should be added.

478 For a general understanding, distribution of the depth-integrated NIKE averaged over
 479 a 10-day period from August 25 to September 4 is presented in Figure 8a. The wind power
 480 integrated over the same period is plotted in Figure 8b. It is clearly shown in Figure 8a that
 481 the high NIKE region mainly located in the offshore waters of Delmarva Peninsula and New
 482 Jersey rather than in the nearshore area. This distribution pattern is rather similar to that of

483 the wind energy input, as presented in Figure 8b, indicating that the NIKE was immediately
 484 gained from the wind power (Rayson et al. 2015; Shen et al., 2017; Zhang et al., 2018). In
 485 fact, the NIKE could also come from other processes apart from the wind energy input
 486 (Alford et al, 2016), meanwhile the wind energy input may also be transferred to energy of
 487 waves apart from NIC (Chen at el., 2017), which leads to differences between Figure 8a and
 488 7b.
 489



490
 491 Figure 8. Spatial distribution of (a) depth-integrated near inertial kinetic energy averaged
 492 over the 10-day period and (b) wind power input to NICs integrated over the 10-day period.
 493

494 An important objective of the present study is to identify the mechanism of NIC
 495 development and decay. For this purpose, we consider a rectangular domain and separate it
 496 into deep water region A (depth > 200 m) and continental shelf region B (depth ≤ 200 m),
 497 as depicted in Figure 1a. If the NICs are considered to be negligibly weak before and after
 498 Hurricane Irene (2011), we may try to find how the wind power that drives the NICs during
 499 the hurricane event is balanced, by comparing the accumulated contribution of different
 500 mechanisms. Performing an integration of each terms in Eq. (13) with respect to time over
 501 10 days from August 25 to September 4 and with respect to the horizontal coordinates over
 502 both deep water region A and continental shelf region B, the contribution of each mechanism
 503 to the energy budget is obtained as shown in Table 1. It is clearly demonstrated that in the

504 deep water region, the wind energy input was basically balanced by the vertical diffusion
505 due to turbulence (40%) and a downward transfer of the near inertial energy to the deep
506 ocean (33%). In the continental shelf region, the vertical diffusion due to turbulence
507 dominated the dissipation of NIKE (nearly 70%), while the bottom friction played a
508 secondary role (24%). It is worthwhile mentioning that lateral divergence of NIKE should
509 not be neglected in both shallow and deep water regions under the hurricane condition
510 (nearly 20%), different from previous studies which focused on NICs under the local wind
511 condition or in a broader research region across the whole North Atlantic (Chant, 2001; Zhai
512 et al., 2009; Shen et al., 2017). Other processes, e.g., advection due to sub-inertial flows,
513 only played a minor role. Note that the ratio of near inertial energy decay to wind energy
514 input exceeded 100% in the continental shelf region, confirming that NIKE may be gained
515 from other sources in addition to wind energy input in nearshore regions (Alford et al., 2016).
516

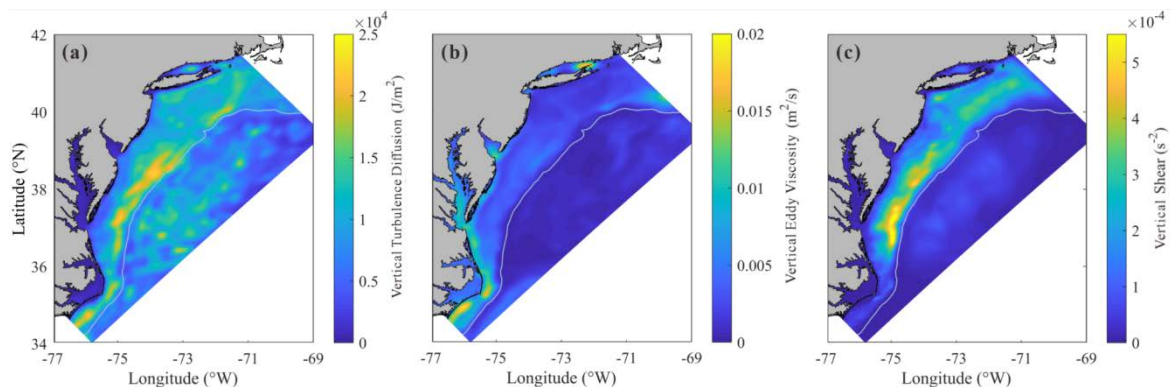
517 Table 1. The contribution of each mechanism to energy budget. Percentages in parentheses
518 refer to the ratio of each factor to wind energy input.

Factor (J)	Contribution in Region A	Contribution in Region B
Wind Energy Input	7.75×10^{14}	3.16×10^{14}
Vertical Turbulence Diffusion	3.12×10^{14} (40%)	2.12×10^{14} (67%)
Lateral Divergence	1.34×10^{14} (17%)	5.69×10^{13} (18%)
Downward Transfer	2.58×10^{14} (33%)	0
Advection	3.33×10^{13} (4%)	1.04×10^{13} (3%)
Conversion	6.9×10^{12} (1%)	1.58×10^{13} (5%)
Bottom Friction	0	7.58×10^{13} (24%)

519
520

521 4.2 Decay of NIKE

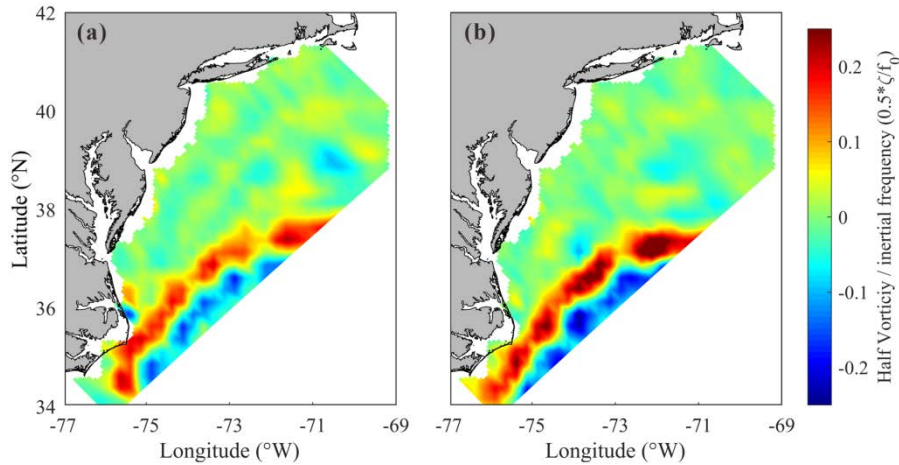
522 The spatial distribution of the time-integrated energy dissipated through vertical
 523 diffusion due to turbulence is plotted in Figure 9a. It is seen that a large amount of the
 524 dissipation occurred at the offshore side of the continental shelf (i.e., at the offshore side of
 525 the shallow region B), which does not coincide with the region where the wind energy input
 526 is intense as demonstrated in Figure 8b. This implies that dissipation of NIKE is not mainly
 527 caused by an increased intensity of turbulence, which certainly takes place in a region where
 528 wind energy input achieves a high level (Zhai et al., 2009; Zhang et al., 2018). For a more
 529 detailed discussion, the averaged eddy viscosity ν_e and the averaged vertical shear rate of
 530 NIC $|\partial \mathbf{u}' / \partial z|^2$ during the period of our study are presented in Figure 9b and 8c. It is then
 531 confirmed that the strong vertical shear also occurred at the outer half of the continental
 532 shelf. The eddy viscosity, however, has a completely different distribution. In conclusion,
 533 the vertical shear, known to be closely related to the ocean stratification (Shen et al., 2017),
 534 plays a crucial role in the turbulence diffusion. It happened that one of the well-known
 535 sharpest thermoclines in the world exists in the coastal water of MAB (Schofield et al., 2008;
 536 Lentz, 2017). It may be necessary to emphasize that, although the stratification in the
 537 shallowest water was totally destroyed during the hurricane event, as mentioned in Section
 538 3, the seawater at the outer half of the continental shelf still partly maintained its
 539 stratification.



540
 541 Figure 9. Spatial distribution of (a) depth-integrated vertical diffusion due to turbulence
 542 integrated over the 10-day period, (b) depth-averaged vertical eddy viscosity and (c) depth-
 543 averaged vertical shear, both averaged over the 10-day period.

544 The lateral divergence of NIKE flux, which also results in decay of NIKE and is not
545 trivial (~20%) in both shallow and deep water regions, may have to be discussed in some
546 details. As shown in Eq. (13), the lateral divergence of NIKE flux is a vertical integration
547 of $\nabla \cdot (\mathbf{u}'p')$, which may also be expressed as an equivalent integration of $\nabla \cdot (\mathbf{c}'E')$,
548 where \mathbf{c}' is the transport velocity of NIKE in the horizontal plane (Price, 1994). When
549 compared to previous studies (Zhai et al., 2009), which dealt with the normal wind induced
550 NIC over a large part of the North Atlantic and showed that the lateral divergence accounted
551 only for less than 5% of the total NIKE loss, we focused only on the hurricane-affected
552 region. In the hurricane-affected region, the larger NIKE gradient naturally leads to a larger
553 divergence. If we extend the domain of study by a factor of 1.5, however, contribution of
554 the averaged lateral divergence decreases by more than half. It is thus strongly implied that
555 the lateral divergence of NIKE flux is significant within the hurricane-affected region.

556 It is also of interest to note that the contribution of the lateral divergence in south region
557 of our computational domain is less than 8%, much smaller than the average value of ~20%.
558 Several studies have pointed out that the transport velocity \mathbf{c}' is largely influenced by the
559 background vorticity gradient (Zhai et al., 2009; Park et al., 2009). In other words, NIKE
560 can hardly be transferred from a place of lower background vorticity to a place of higher
561 background vorticity or, NIKE can hardly penetrate a vorticity ridge from either side. Shown
562 in Figure 10 is the distribution of the background vorticity within our computational domain
563 during the hurricane event (data from [https://resources.marine.copernicus.eu/product-
564 detail/SEALEVEL_GLO_PHY_CLIMATE_L4_MY_008_057/INFORMATION](https://resources.marine.copernicus.eu/product-detail/SEALEVEL_GLO_PHY_CLIMATE_L4_MY_008_057/INFORMATION)). A
565 remarkable vorticity ridge exists in the southeast of the computational domain, which is
566 considered to be caused by the strong horizontal shear at the edge of Gulf Stream (a warm
567 and swift ocean current in Atlantic, flowing through the southern MAB and propagating
568 northeastward). This vorticity ridge can reduce the lateral divergence of NIKE flux in south
569 region of our computational domain.



570

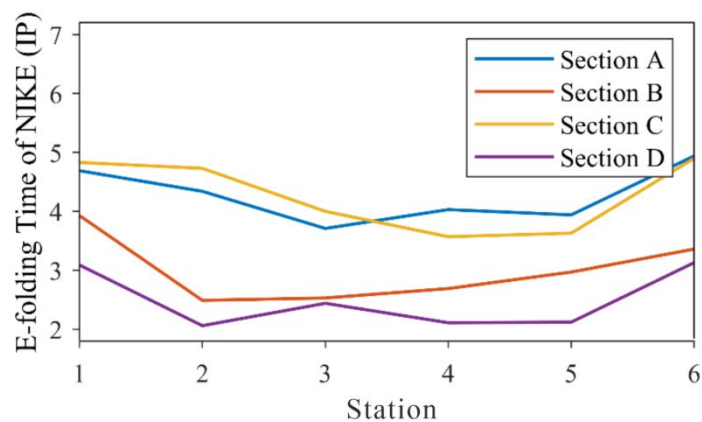
571 Figure 10. Spatial distribution of background vorticity (a) before the hurricane event on Aug
 572 25 and (b) after the hurricane event on Sep 4.

573

574 4.3 Decay timescale of NIKE

575 It is of practical importance to determine the rate of NIKE decay. A conventional
 576 measure of the rate of NIKE may be its e-folding time, i.e., the timescale in which the NIKE
 577 decreases by a factor of e . Shown in Figure 11 is the e-folding time of the depth-integrated
 578 NIKE at 24 stations along sections A to D. The decay timescale in section E is not considered
 579 because this section is relatively far from the hurricane track as compared with other
 580 sections and also because the orientation of section E differs quite significantly from that of
 581 other sections.

582



583

584 Figure 11. The decay timescale of the depth-integrated NIKE at 24 stations along sections
 585 A to D. Note that the unit for the e-folding time is the inertial period.

586 It is interesting to note that the decay timescales in the shallow and deep regions are
587 fairly different. As shown in Figure 11, the NIKE is dissipated much more slowly outside
588 the shelf break (Station No.6) than over the continental shelf. This difference is often
589 considered to be an effect of the bottom friction and the extremely strong turbulence in the
590 shallow waters, as pointed out by other researchers (Rayson et al., 2015; Shen et al., 2017).
591 It is also interesting to find that the variation of NIKE decay rate in shallow waters is much
592 more complicated than in the deep waters. In the cross-shore direction, the NIKE at the
593 middle stations, i.e., Stations No. 3 to No. 5, located at the outer half of the continental shelf,
594 is shown to be dissipated most rapidly, especially along sections A to C (Figure 11). This
595 phenomenon is actually supported by the fact that the strongest turbulence diffusion
596 occurred over the outer half of the continental shelf, particularly in the relevant region
597 between sections A and C (Figure 9a). Considering the variation of the wind energy input
598 within the same section should not be too large, the ratio of turbulence diffusion to wind
599 energy input must be mainly determined by the turbulence diffusion. Therefore, the strong
600 turbulence dissipation due to the strong vertical shear in well-maintained stratification is
601 responsible for the rapid energy decay in the outer half of the continental shelf, as shown in
602 Section 4.2. Although the bottom friction also has some effect on the decay timescale of
603 NIKE onshore, the turbulence effect is predominant.

604 In the alongshore direction, it is shown that the NIKE in sections B and D decayed
605 more rapidly. Actually, the decay timescale there is only 2 to 3 inertial periods compared to
606 4 to 5 inertial periods in sections A and C. However, the limited variability of the turbulence
607 diffusion in alongshore direction should not lead to such a big difference. Near section A,
608 the vorticity ridge in Gulf Stream restricted the lateral divergence of NIKE, which may
609 contribute to a long decay timescale to some extent. However, the role of this effect was
610 limited. In fact, as mentioned in Section 3, the nonlinear wave-wave interaction near section
611 B may have caused a transfer of NIKE to other frequencies, as also pointed out by Shen et
612 al. (2017). In fact, it is found that the ratio of turbulence diffusion to wind input in section
613 B was larger than in other sections by 20%-30%, due to the low level of wind input (Figure

614 8b) and high level of turbulence dissipation (Figure 9a) there. These factors combined seem
615 to have yielded an extraordinarily short e-folding time in section B. In section D, due to the
616 complete destruction of stratification after the hurricane event (as mentioned in Section 3
617 and shown in Figure 7d), the NICs were of the same order as the background flow (D1-D4
618 in Figure 6). Therefore, the decay timescale of NIKE in section D is certainly inaccurate
619 and possibly meaningless.

620 **5 Conclusion**

621 This study is aimed to investigate the development and decay mechanism of NICs in
622 the MAB area caused by Hurricane Irene (2011). Numerical results obtained with ROMS
623 are shown to agree well with the observational data. Both computational and observational
624 results show that the rotating wind of the hurricane immediately forced a rotating current in
625 the surface layer of the ocean and induced an inertial current rotating in the opposite
626 direction about one inertial period after the hurricane passed over. The NICs overwhelmed
627 M2 tide in most areas of the MAB region except in the nearshore area where the
628 stratification was totally destroyed by the strong mixing due to turbulence. In addition, the
629 cross-shore component of the NIC velocity gradually increases by a factor of at least three
630 from a shallow-water position to the shelf break.

631 The energy budget in the NICs is investigated in both deep and shallow waters. NIKE
632 was shown to be immediately gained from the wind power during the hurricane event. In
633 the deep water region, NIKE was mainly dissipated by the vertical diffusion due to
634 turbulence and partially transferred to deep waters. In the continental shelf region, NIKE
635 was basically dissipated by the turbulence diffusion, meanwhile the bottom friction played
636 a secondary role. The nonlinear wave-wave interaction only dissipated NIKE in limited
637 regions, e.g. shelf waters off Delmarva Peninsula. Notably, the lateral divergence of NIKE
638 should be taken into consideration in both shallow and deep water regions under the
639 hurricane condition. However, in southern MAB, it was restricted by a vorticity ridge at the
640 edge of Gulf Stream. It is also clarified that the NIKE dissipation due to turbulence diffusion

641 is much more closely related to the rate of the vertical shear rather than the intensity of
642 turbulence, which certainly takes place in a region where wind energy input achieves a high
643 level. The strong vertical shear at the offshore side of the continental shelf led to the
644 strong turbulence dissipation in this region.

645 **Acknowledgements**

646 This research is supported by National Natural Science Foundation of China (NSFC)
647 under grant No. 11732008.

648 **Data Availability Statements**

649 The data used in this study are listed below. In particular, the regional oceanic modeling
650 system (ROMS) code is available at <https://www.myroms.org>; HF radar data is available at
651 [http://tds.marine.rutgers.edu/thredds/dodsC/cool/codar/totals/5Mhz_6km_realtime_fmrc/
652 Maracoos_5MHz_6km_Totals-FMRC_best.ncd.html](http://tds.marine.rutgers.edu/thredds/dodsC/cool/codar/totals/5Mhz_6km_realtime_fmrc/Maracoos_5MHz_6km_Totals-FMRC_best.ncd.html); Glider data is available at
653 [http://tds.marine.rutgers.edu/thredds/dodsC/cool/glider/mab/Gridded/20110810T1330_epa
654 _ru16_active.nc.html](http://tds.marine.rutgers.edu/thredds/dodsC/cool/glider/mab/Gridded/20110810T1330_epa_ru16_active.nc.html); HYCOM data is available at [https://www.hycom.org/data/glb0pt08/
655 expt-91pt2](https://www.hycom.org/data/glb0pt08/expt-91pt2); ADCIRC data is available at <https://adcirc.org/products/adcirc-tidal-databases>;
656 USGS data is available at <https://waterdata.usgs.gov>; H*WIND data is available at
657 https://www.aoml.noaa.gov/hrd/data_sub/wind.html; NAM data is available at
658 [https://www.ncdc.noaa.gov/data-access/model-data/model-datasets/north-american-
659 mesoscale-forecast-system-nam](https://www.ncdc.noaa.gov/data-access/model-data/model-datasets/north-american-mesoscale-forecast-system-nam); C3S data is available at
660 [https://resources.marine.copernicus.eu/product-detail/SEALEVEL_GLO_PHY
661 _CLIMATE_L4_MY_008_057/INFORMATION](https://resources.marine.copernicus.eu/product-detail/SEALEVEL_GLO_PHY_CLIMATE_L4_MY_008_057/INFORMATION); AVHRR data is available at
662 <https://earth.esa.int/eogateway/catalog/avhrr-level-1b-local-area-coverage-imagery>.

663 **References**

664 Alford, M.H., 2003a. Improved global maps and 54-year history of wind-work on ocean
665 inertial motions. *Geophysical Research Letters*, 30(8).

666 Alford, M.H., 2003b. Redistribution of energy available for ocean mixing by long-range
667 propagation of internal waves. *Nature*, 423(6936): 159-162.

668 Alford, M.H., MacKinnon, J.A., Simmons, H.L. and Nash, J.D., 2016. Near-inertial internal
669 gravity waves in the ocean. *Annual Review of Marine Science*, 8(1): 95-123.

670 Allahdadi, M., 2014. Numerical experiments of hurricane impact on vertical mixing and de-
671 stratification of the louisiana shelf waters. Ph. D. Thesis, Louisiana State University,
672 Baton Rouge.

673 Amante, C. and Eakins, B.W., 2009. Etopo1 1 arc-minute global relief model: Procedures,
674 data sources and analysis. NOAA Technical Memorandum NESDIS NGDC-24,
675 National Geophysical Data Center, NOAA.

676 Avila, L.A. and Cangialosa, J., 2011. Tropical cyclone report: Hurricane irene: August 21–
677 28, 2011. National Hurricane Center Report AL0920011, US National Oceaninc and
678 Atmospheric Administration's National Weather Service.

679 Brunner, K. and Lwiza, K.M.M., 2020. Tidal velocities on the mid-atlantic bight continental
680 shelf using high-frequency radar. *Journal of Oceanography*, 76(4): 289-306.

681 Castelao, R.M., 2014. Mesoscale eddies in the south atlantic bight and the gulf stream
682 recirculation region: Vertical structure. *Journal of Geophysical Research: Oceans*,
683 119(3): 2048-2065.

684 Chang, S.W. and Anthes, R.A., 1978. Numerical simulations of the ocean's nonlinear,
685 baroclinic response to translating hurricanes. *Journal of Physical Oceanography*,
686 8(3): 468-480.

687 Chant, R.J., 2001. Evolution of near-inertial waves during an upwelling event on the new
688 jersey inner shelf. *Journal of Physical Oceanography*, 31(3): 746-764.

689 Chassignet, E.P. et al., 2007. The hycom (hybrid coordinate ocean model) data assimilative
690 system. *Journal of Marine Systems*, 65(1): 60-83.

691 Chen, C., Reid, R.O. and Nowlin Jr, W.D., 1996. Near-inertial oscillations over the texas-
692 louisiana shelf. *Journal of Geophysical Research: Oceans*, 101(C2): 3509-3524.

693 Chen, C. and Xie, L., 1997. A numerical study of wind-induced, near-inertial oscillations

694 over the texas-louisiana shelf. *Journal of Geophysical Research: Oceans*, 102(C7):
695 15583-15593.

696 Chen, G., Xue, H., Wang, D. and Xie, Q., 2013. Observed near-inertial kinetic energy in the
697 northwestern south china sea. *Journal of Geophysical Research: Oceans*, 118(10):
698 4965-4977.

699 Chen, S., Chen, D. and Xing, J., 2017. A study on some basic features of inertial oscillations
700 and near-inertial internal waves. *Ocean Science*, 13(5): 829-836.

701 Chen, Y. and Yu, X., 2016. Enhancement of wind stress evaluation method under storm
702 conditions. *Climate Dynamics*, 47(12): 3833-3843.

703 Chen, Y., Zhang, F., Green, B.W. and Yu, X., 2018. Impacts of ocean cooling and reduced
704 wind drag on hurricane katrina (2005) based on numerical simulations. *Monthly
705 Weather Review*, 146(1).

706 Churchill, J.H., Wirick, C.D., Flagg, C.N. and Pietrafesa, L.J., 1994. Sediment resuspension
707 over the continental shelf east of the delmarva peninsula. *Deep Sea Research Part II:
708 Topical Studies in Oceanography*, 41(2): 341-363.

709 Cummings, J.A., 2005. Operational multivariate ocean data assimilation. *Quarterly Journal
710 of the Royal Meteorological Society*, 131(613): 3583-3604.

711 D'Asaro, E.A., 1985. The energy flux from the wind to near-inertial motions in the surface
712 mixed layer. *Journal of Physical Oceanography*, 15: 1043-1059.

713 Davies, A.M. and Xing, J., 2003. On the interaction between internal tides and wind-induced
714 near-inertial currents at the shelf edge. *Journal of Geophysical Research: Oceans*,
715 108(C3).

716 Derrick, T.R., Bates, B.T. and Dufek, J.S., 1994. Evaluation of time-series data sets using
717 the pearson product-moment correlation coefficient. *Medicine and science in sports
718 and exercise*, 26(7): 919-928.

719 Donelan, M.A. et al., 2004. On the limiting aerodynamic roughness of the ocean in very
720 strong winds. *Geophysical Research Letters*, 31(18).

721 Dorostkar, A., Boegman, L., Diamessis, P. and Pollard, A., 2010. Sensitivity of mitgcm to

722 different model parameters in application to Cayuga Lake. Proceedings of the 6th
723 International Symposium on Environmental Hydraulics, Two Volume Set, pp.
724 373-378.

725 Emanuel, K.A., 1995. Sensitivity of tropical cyclones to surface exchange coefficients and
726 a revised steady-state model incorporating eye dynamics. *Journal of the*
727 *Atmospheric Sciences*, 52: 3969-3976.

728 Fairall, C.W., Bradley, E.F., Rogers, D.P., Edson, J.B. and Young, G.S., 1996. Bulk
729 parameterization of air-sea fluxes for tropical ocean-global atmosphere coupled-
730 ocean atmosphere response experiment. *Journal of Geophysical Research: Oceans*,
731 101(C2): 3747-3764.

732 Freeman, N.G., Hale, A.M. and Danard, M.B., 1972. A modified sigma equations' approach
733 to the numerical modeling of Great Lakes hydrodynamics. *Journal of Geophysical*
734 *Research* 77(6): 1050-1060.

735 Furuichi, N., Hibiya, T. and Niwa, Y., 2008. Model-predicted distribution of wind-induced
736 internal wave energy in the world's oceans. *Journal of Geophysical Research:*
737 *Oceans*, 113(C9).

738 Garrett, C., 2001. What is the "near-inertial" band and why is it different from the rest of
739 the internal wave spectrum? *Journal of Physical Oceanography*, 31(4): 962-971.

740 Glenn, S.M. et al., 2016. Stratified coastal ocean interactions with tropical cyclones. *Nature*
741 *Communications*, 7(1): 10887.

742 Gregg, M.C., 1987. Diapycnal mixing in the thermocline: A review. *Journal of Geophysical*
743 *Research: Oceans*, 92(C5): 5249-5286.

744 Haidvogel, D.B. et al., 2008. Ocean forecasting in terrain-following coordinates:
745 Formulation and skill assessment of the regional ocean modeling system. *Journal of*
746 *Computational Physics*, 227(7): 3595-3624.

747 Hoarfrost, A. et al., 2019. Gulf Stream ring water intrusion on the mid-Atlantic Bight
748 continental shelf break affects microbially driven carbon cycling. 6.

749 Holliday, D. and McIntyre, M.E., 1981. On potential energy density in an incompressible,

750 stratified fluid. *Journal of Fluid Mechanics*, 107: 221-225.

751 Hopkins, J.E., Stephenson Jr, G.R., Green, J.A.M., Inall, M.E. and Palmer, M.R., 2014.
752 Storms modify baroclinic energy fluxes in a seasonally stratified shelf sea: Inertial-
753 tidal interaction. *Journal of Geophysical Research: Oceans*, 119(10): 6863-6883.

754 Hormann, V., Centurioni, L.R., Rainville, L., Lee, C.M. and Braasch, L.J., 2014. Response
755 of upper ocean currents to typhoon fanapi. *Geophysical Research Letters*, 41(11):
756 3995-4003.

757 Jackett, D.R. and McDougall, T.J., 1995. Minimal adjustment of hydrographic profiles to
758 achieve static stability. *Journal of Atmospheric and Oceanic Technology*, 12(2): 381-
759 389.

760 Janjic, Z.I. et al., 2004, June. The ncep wrf core, 20th Conference on Weather Analysis and
761 Forecasting/16th Conference on Numerical Weather Prediction, Seattle, Washington,
762 pp. 10-25.

763 Jochum, M. et al., 2013. The impact of oceanic near-inertial waves on climate. *Journal of*
764 *Climate*, 26(9): 2833-2844.

765 Kang, D. and Fringer, O., 2010. On the calculation of available potential energy in internal
766 wave fields. *Journal of Physical Oceanography*, 40(11): 2539-2545.

767 Kawaguchi, Y., Wagawa, T. and Igeta, Y., 2020. Near-inertial internal waves and multiple-
768 inertial oscillations trapped by negative vorticity anomaly in the central sea of japan.
769 *Progress in Oceanography*, 181: 102240.

770 Kim, S.Y. and Kosro, P.M., 2013. Observations of near-inertial surface currents off oregon:
771 Decorrelation time and length scales. *Journal of Geophysical Research: Oceans*,
772 118(7): 3723-3736.

773 Kohut, J., Roarty, H., Randall-Goodwin, E., Glenn, S. and Lichtenwalner, C.S., 2012.
774 Evaluation of two algorithms for a network of coastal HF Radars in the Mid-Atlantic
775 Bight. *Ocean Dynamics*, 62(6): 953-968.

776 Kunze, E., 1985. Near-inertial wave propagation in geostrophic shear. *Journal of Physical*
777 *Oceanography*, 15(5): 544-565.

778 Lentz, S.J., 2017. Seasonal warming of the middle atlantic bight cold pool. *Journal of*
779 *Geophysical Research: Oceans*, 122(2): 941-954.

780 Li, M., Zhong, L., Boicourt, W.C., Zhang, S. and Zhang, D.-L., 2007. Hurricane-induced
781 destratification and restratification in a partially-mixed estuary. *Journal of Marine*
782 *Research*, 65(2): 169-192.

783 MacCready, P. and Giddings, S.N., 2016. The mechanical energy budget of a regional ocean
784 model. *Journal of Physical Oceanography*, 46(9): 2719-2733.

785 MacKinnon, J.A. and Gregg, M.C., 2005. Near-inertial waves on the new england shelf:
786 The role of evolving stratification, turbulent dissipation, and bottom drag. *Journal*
787 *of Physical Oceanography*, 35(12): 2408-2424.

788 Marchesiello, P., McWilliams, J.C. and Shchepetkin, A., 2001. Open boundary conditions
789 for long-term integration of regional oceanic models. *Ocean Modelling*, 3(1): 1-20.

790 Miles, T., Seroka, G. and Glenn, S., 2017. Coastal ocean circulation during hurricane sandy.
791 *Journal of Geophysical Research: Oceans*, 122(9): 7095-7114.

792 Mulligan, R.P. and Hanson, J.L., 2016. Alongshore momentum transfer to the nearshore
793 zone from energetic ocean waves generated by passing hurricanes. *Journal of*
794 *Geophysical Research: Oceans*, 121(6): 4178-4193.

795 Munk, W. and Wunsch, C., 1998. Abyssal recipes ii: Energetics of tidal and wind mixing.
796 *Deep Sea Research Part I: Oceanographic Research Papers*, 45(12): 1977-2010.

797 Olabarrieta, M., Warner, J.C. and Kumar, N., 2011. Wave-current interaction in willapa bay.
798 *Journal of Geophysical Research: Oceans*, 116(C12).

799 Park, J.J., Kim, K. and Schmitt, R.W., 2009. Global distribution of the decay timescale of
800 mixed layer inertial motions observed by satellite-tracked drifters. *Journal of*
801 *Geophysical Research: Oceans*, 114(C11).

802 Pollard, R.T., 1980. Properties of near-surface inertial oscillations. *Journal of Physical*
803 *Oceanography*, 10(3): 385-398.

804 Powell, M.D., Houston, S.H., Amat, L.R. and Morisseau-Leroy, N., 1998. The hrd real-time
805 hurricane wind analysis system. *Journal of Wind Engineering and Industrial*

806 Aerodynamics, 77-78: 53-64.

807 Powell, M.D., Vickery, P.J. and Reinhold, T.A., 2003. Reduced drag coefficient for high
808 wind speeds in tropical cyclones. *Nature*, 422(6929): 279-283.

809 Price, J.F., 1983. Internal wave wake of a moving storm. Part i. Scales, energy budget and
810 observations. *Journal of Physical Oceanography*, 13(6): 949-965.

811 Price, J.F., Sanford, T.B. and Forristall, G.Z., 1994. Forced stage response to a moving
812 hurricane. *Journal of Physical Oceanography*, 24(2): 233-260.

813 Rayson, M.D. et al., 2015. Near-inertial ocean response to tropical cyclone forcing on the
814 australian north-west shelf. *Journal of Geophysical Research: Oceans*, 120(12):
815 7722-7751.

816 Rimac, A., von Storch, J.-S., Eden, C. and Haak, H., 2013. The influence of high-resolution
817 wind stress field on the power input to near-inertial motions in the ocean.
818 *Geophysical Research Letters*, 40(18): 4882-4886.

819 Roarty, H. et al., 2010. Operation and application of a regional high-frequency radar
820 network in the mid-atlantic bight. *Marine Technology Society Journal*, 44(6): 133-
821 145.

822 Roarty, H. et al., 2020. Annual and seasonal surface circulation over the mid-atlantic bight
823 continental shelf derived from a decade of high frequency radar observations.
824 *Journal of Geophysical Research: Oceans*, 125(11): e2020JC016368.

825 Rodi, W., 1987. Examples of calculation methods for flow and mixing in stratified fluids.
826 *Journal of Geophysical Research: Oceans*, 92(C5): 5305-5328.

827 Sanford, T.B., Price, J.F. and Girton, J.B., 2011. Upper-ocean response to hurricane frances
828 (2004) observed by profiling em-apex floats. *Journal of Physical Oceanography*,
829 41(6): 1041-1056.

830 Schofield, O. et al., 2008. The decadal view of the mid-atlantic bight from the coolroom: Is
831 our coastal system changing? *Oceanography*, 21(4): 108-117.

832 Schofield, O. et al., 2007. Slocum gliders: Robust and ready. *Journal of Field Robotics*,
833 24(6): 473-485.

834 Schofield, O. et al., 2010. A regional slocum glider network in the Mid-Atlantic Bight
835 leverages broad community engagement. *Marine Technology Society Journal*, 44(6):
836 185-195.

837 Seroka, G. et al., 2016. Hurricane Irene sensitivity to stratified coastal ocean cooling.
838 *Monthly Weather Review*, 144(9): 3507-3530.

839 Seroka, G. et al., 2017. Rapid shelf-wide cooling response of a stratified coastal ocean to
840 hurricanes. *Journal of Geophysical Research: Oceans*, 122(6): 4845-4867.

841 Shchepetkin, A.F. and McWilliams, J.C., 2005. The regional oceanic modeling system
842 (roms): A split-explicit, free-surface, topography-following-coordinate oceanic
843 model. *Ocean Modelling*, 9(4): 347-404.

844 Shearman, R.K., 2005. Observations of near-inertial current variability on the new england
845 shelf. *Journal of Geophysical Research: Oceans*, 110(C2).

846 Shen, J., Qiu, Y., Zhang, S. and Kuang, F., 2017. Observation of tropical cyclone-induced
847 shallow water currents in taiwan strait. *Journal of Geophysical Research: Oceans*,
848 122(6): 5005-5021.

849 Steiner, A. et al., 2017. Critical weather situations for renewable energies-part a: Cyclone
850 detection for wind power. *Renewable Energy*, 101: 41-50.

851 Stommel, H., 2020. *The Gulf Stream*. University of California Press.

852 Thiebaut, S. and Vennell, R., 2010. Observation of a fast continental shelf wave generated
853 by a storm impacting newfoundland using wavelet and cross-wavelet analyses.
854 *Journal of Physical Oceanography*, 40(2): 417-428.

855 Thyng, K.M. et al., 2021. Performance of offline passive tracer advection in the regional
856 ocean modeling system (roms; v3.6, revision 904). *Geoscientific Model
857 Development*, 14(1): 391-407.

858 Toffoli, A., McConochie, J., Ghantous, M., Loffredo, L. and Babanin, A.V., 2012. The effect
859 of wave-induced turbulence on the ocean mixed layer during tropical cyclones: Field
860 observations on the australian north-west shelf. *Journal of Geophysical Research:
861 Oceans*, 117(C11).

862 Umlauf, L. and Burchard, H., 2003. A generic length-scale equation for geophysical
863 turbulence models. *Journal of Marine Research*, 61(2): 235-265.

864 Warner, J.C., Defne, Z., Haas, K. and Arango, H.G., 2013. A wetting and drying scheme for
865 roms. *Computers & Geosciences*, 58: 54-61.

866 Wu, R., Zhang, H. and Chen, D., 2020. Effect of typhoon kalmaegi (2014) on northern south
867 china sea explored using multi-platform satellite and buoy observations data.
868 *Progress in Oceanography*, 180: 102218.

869 Xu, J., Chao, S.-Y., Hood, R.R., Wang, H.V. and Boicourt, W.C., 2002. Assimilating high-
870 resolution salinity data into a model of a partially mixed estuary. *Journal of*
871 *Geophysical Research: Oceans*, 107(C7): 11-1-11-14.

872 Xu, Y. and Yu, X., 2021. Enhanced atmospheric wave boundary layer model for evaluation
873 of wind stress over waters of finite depth. *Progress in Oceanography*, 198: 102664.

874 Yang, B., Hou, Y., Hu, P., Liu, Z. and Liu, Y., 2015. Shallow ocean response to tropical
875 cyclones observed on the continental shelf of the northwestern south china sea.
876 *Journal of Geophysical Research: Oceans*, 120(5): 3817-3836.

877 Zhai, X., Greatbatch, R.J., Eden, C. and Hibiya, T., 2009. On the loss of wind-induced near-
878 inertial energy to turbulent mixing in the upper ocean. *Journal of Physical*
879 *Oceanography*, 39(11): 3040-3045.

880 Zhang, F., Li, M. and Miles, T., 2018. Generation of near-inertial currents on the Mid-
881 Atlantic Bight by Hurricane Arthur (2014). *Journal of Geophysical Research:*
882 *Oceans*, 123(4): 3100-3116.

883 Zhang, H. et al., 2016. Upper ocean response to Typhoon Kalmaegi (2014). *Journal of*
884 *Geophysical Research: Oceans*, 121(8): 6520-6535.

885